

Multiferroic Micro-Motors With Deterministic Single Input Control

John P. Domann*

*Department of Biomedical Engineering and Mechanics,
Virginia Polytechnic and State University*

Cai Chen, Abdon E. Sepulveda, and Greg P. Carman
*Department of Mechanical and Aerospace Engineering,
University of California, Los Angeles*

Rob N. Candler

*Department of Electrical and Computer Engineering,
University of California, Los Angeles
Department of Mechanical and Aerospace Engineering,
University of California, Los Angeles and
California NanoSystems Institute, Los Angeles*

(Dated: February 27, 2018)

Abstract

Abstract:

This paper describes a method for achieving continuous deterministic 360° magnetic moment rotations in single domain magnetoelastic discs, and examines the performance bounds for a mechanically lossless multiferroic bead-on-a-disc motor based on dipole coupling these discs to small magnetic nanobeads. The continuous magnetic rotations are attained by controlling the relative orientation of a four-fold anisotropy (e.g., cubic magnetocrystalline anisotropy) with respect to the two-fold magnetoelastic anisotropy. This approach produces continuous rotations from the quasi-static regime up through operational frequencies of several GHz. Driving strains of only ≈ 90 to 180 ppm are required for operation of motors using existing materials. The large operational frequencies and small sizes, with lateral dimensions of ≈ 100 s of nanometers, produce large power densities for the rotary bead-on-a-disc motor, and a newly proposed linear variant, in a size range where power dense alternative technologies do not currently exist.

Keywords: motor, multiferroic, piezoelectric, magnetoelastic, magnetostriction, anisotropy, deterministic control

* jpdomann@vt.edu

I. BACKGROUND / LITERATURE REVIEW

In his 1842 lecture *On a new Class of Magnetic Forces* James Joule describes how following the suggestion of an "ingenuous gentleman," he initiated the first ever measurements of magnetoelasticity.[1] From the outset, Joule was focused on determining not just if a bar of iron would elongate in the presence of a magnetic field, but if "power could be advantageously employed for the movement of machinery." In other words, Joule was interested in making magnetoelastic motors. However, after measuring a magnetic field induced strain of only $\epsilon \approx 1.4$ ppm, Joule concluded that "With regard to the application of the new force to the movement of machinery, I have nothing favourable to advance."

Of course, in that very same lecture Joule was doubtful that electromagnetic motors had any future use, showing a slight lack of foresight in an otherwise exemplary career. While many different types of motors have been created, macro-scale combustion and electromagnetic motors are the most widely used. However, poor scaling laws rapidly degrade the performance of these traditional motor technologies at the microscale, and new approaches need to be considered. Figure 1a highlights the available power density for a variety of different micro and nanoscale motor technologies. For reference, the combustion engine of a 2017 Ford Mustang can generate around 400 horsepower (300 kW) and is sized on the order of 1 m^3 , generating a power density of 300 kW m^{-3} (i.e., moderate to high power density but at significantly larger sizes than shown on Figure 1a).

The larger sizes on Figure 1a are representative of MEMS motors with volumes $\approx 1 \text{ mm}^3$. The data points come from numerous different technological approaches, including electrostatic,[2–8] magnetostatic,[9, 10] electromagnetic,[11] electrohydrodynamic,[12] piezoelectric,[13–22] pneumatic,[23–27] and plasmonic[28, 29] technology bases. These motors can advantageously be controlled with conventional electronic systems; however the power density of existing MEMS approaches clearly doesn't scale well to sizes significantly smaller than a cubic millimeter.

At volumes near 1 nm^3 , molecular motors like rotaxane are extremely power dense. These molecules generate forces near 30 pN, with strokes of 5 nm, at rates of up to 3 kHz. This produces power densities on the order of 100 GW m^{-3} . [30, 31] In addition to rotaxane, molecular motors based on nanocrystal actuators,[32, 33] and ATP synthase[35, 36] have been created. However, molecular motors are exceedingly difficult to locally control, leading to poor array / scaling properties.

Figure 1a illustrates that there are currently no power dense motor technologies at the μm^3

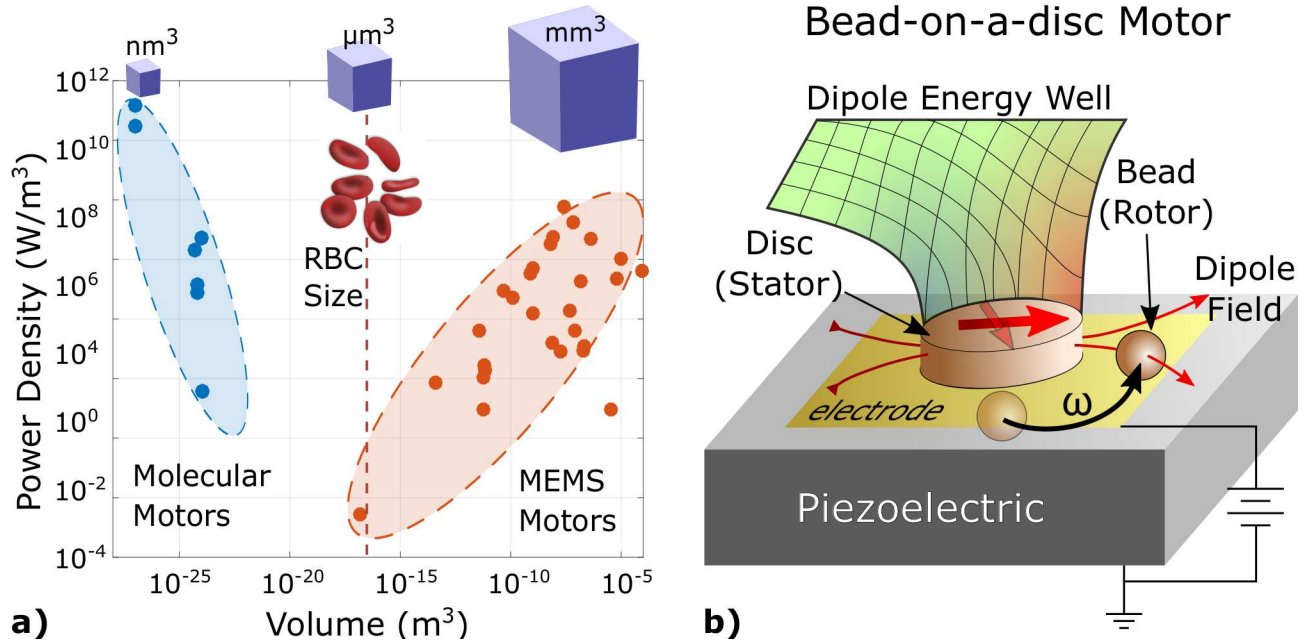


FIG. 1. a) Power density of micro and nanoscale motor technologies, indicating no power dense technologies exist at the μm^3 size scale.[2–36] Shown for scale are several red blood cells (RBCs). b) The proposed multiferroic bead-on-a-disc motor uses dipole coupling to drag a small magnetic bead around a stationary magnetic disc with rotating magnetic moment.

size scale. A μm^3 motor would enable localized control on the same size scale as biological cells, facilitating diagnostic and therapeutic applications in addition to opening new avenues for fundamental research. As an example, Di Carlo et al. have recently demonstrated magnetic cell sorting techniques near the microscale, and improved control could enable the study of individual cellular components instead of relying on traditional cell lysis based techniques.[37]

Multiferroic heterostructures have recently been proposed as highly power dense μm^3 motors.[38] These motors manipulate large magnetic forces by controlling the dipole fields of single domain magnetic heterostructures or domain walls with strain. Multiferroic control is energy efficient[39, 40] even at high frequency operation.[41, 42] These effects should combine to produce large power densities. Figure 1b shows a hypothetical bead-on-a-disk motor,[38] where the magnetic moment of the large disk rotates (the disk itself is stationary), and drags around the smaller bead through dipole coupling. The B-field generated by the large disk applies a torque on the magnetic bead to keep it aligned with the B-field, while ∇B applies a force on the bead and causes it to rotate around the large disk.

A key impediment to the creation of multiferroic motors has been achieving deterministic control of continuous 360° magnetic rotations. Initial studies on magnetoelastic control used single electrodes to cause 90° non-deterministic rotations in ellipse shaped structures.[38, 43, 44] However, the use of a single electrode and elliptical shape is restricted to a maximum rotation of 90° , since it combines two uniaxial (i.e., two-fold) anisotropies (see the Supplementary Information for a mathematical explanation). This restriction motivated subsequent studies with multiple electrodes that generated a rotating biaxial plane strain state.[45, 46] Several modeling efforts have looked at this challenge, and observed that the use of 4 or more electrodes can deterministically control rotations.[47, 48] The multi-electrode approach has resulted in experimental observation of deterministic rotations in increments of 45° confirmed up to 180° .[49] Recent work has also shown dynamic effects can lead to 180° rotations (i.e., ballistic switching with PMA).[50] However, fabricating motor arrays with multiple electrodes is undesirable, and ballistic switching requires precise timing with very narrow-band performance limiting variable frequency use.

A path to single electrode deterministic control with broadband operation can be found in three different studies analyzing the effects of rotating the relative orientation of the magnetoelastic anisotropy with respect to the shape of nanomagnetic structures. This approach has led to model based predictions of deterministic rotations in shapes like four leaf clovers,[51] squares,[52] cat eyes,[53] and peanuts.[53] However, most of these shapes require the use of complex fabrication techniques to resolve fine features, and are prone to the creation of pinning sites that have likely prevented rotation in previous work.[46] To overcome these issues, the present study analyzes a single electrode control method for deterministic 360° rotations, avoiding complex geometries or electrode patterns. A bead-on-a-disk motor is then analyzed and predictions provided for a mechanically lossless motor's performance (i.e., only magnetic and inertial forces are considered in the limit of zero fluidic drag).

II. MODEL

While previous studies have combined magnetoelasticity with an additional two-fold anisotropy (i.e., elliptical shapes), this work combines a four-fold anisotropy (e.g., cubic MCA) with the magnetoelastic anisotropy. This work demonstrates the key to generating deterministic 360° rotations is to rotate the principal orientation of the anisotropies with respect to one another. In the following section the static and dynamic rotational characteristics of the stator element (large magnetic disk)

with rotated anisotropies will be analyzed, then a second section analyzing the upper performance bounds of a bead-on-a-disk motor will be presented.

A. Quasi-Static Energy Analysis

Figure 2 shows the a) dipole field, b) stator geometry, and c) dipole forces for the motor being analyzed. This figure is a top down view of the motor shown in Figure 1b. A circular thin-film

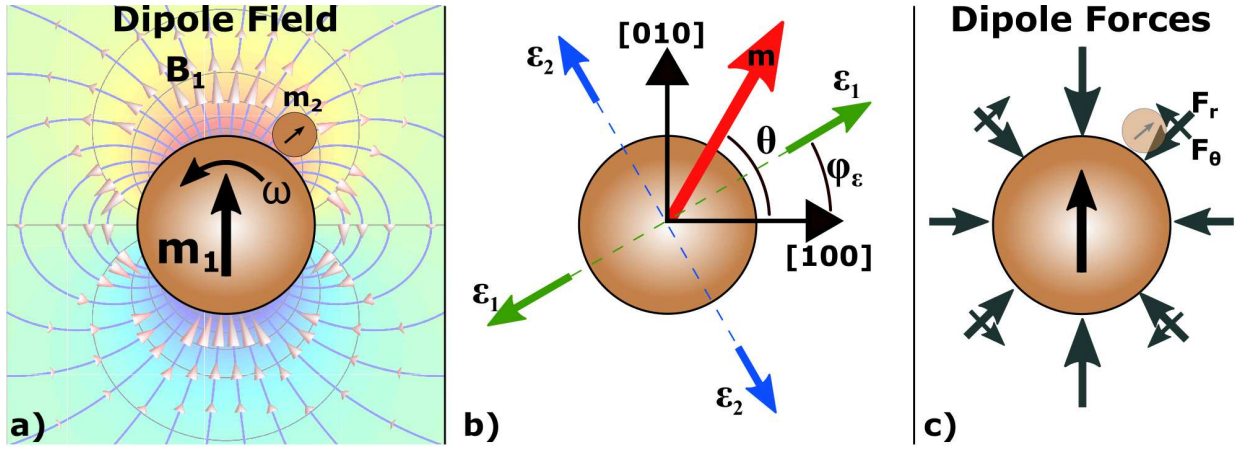


FIG. 2. a) Bead-on-a-disk motor with surrounding magnetic dipole field. The large disk (stator) remains stationary, but its magnetic moment rotates in response to an applied strain. Dipole coupling drags the bead (rotor) around the stator. b) Orientation of the magnetic moment and principal strains. c) Dipolar forces on a bead near the stator element.

stator is studied, with in-plane magnetic orientation θ . The stator is subject to a voltage induced plane strain ($\epsilon_{13} = \epsilon_{23} = \epsilon_{33} = 0$), with principal strains components ϵ_1 and ϵ_2 rotated ϕ_ϵ from the x-axis ([100] direction). While the magnitude and sign of the applied strain may change as a function of time, the orientation is assumed fixed during motor operation (i.e., applied using a single fixed electrode). Further assuming the out-of-plane magnetization m_3 is small due to shape anisotropy, the relevant stator energy density reduces to

$$U_{tot} = U_{MCA} + U_{ME} \quad (1)$$

$$= K_1^{MCA} [m_1^2 m_2^2] + B_1 [\epsilon_{11}(m_1^2 - 1/3) + \epsilon_{22}(m_2^2 - 1/3)] + 2B_2 [\epsilon_{12} m_1 m_2] \quad (2)$$

where U_{tot} , U_{MCA} , and U_{ME} are the total, magnetocrystalline, and magnetoelastic energies, respectively, K_1^{mca} is the first order cubic MCA constant, B_1 and B_2 are the cubic magnetoelastic

anisotropy coefficients, the m_i terms are the magnetization direction cosines, and ε_{ij} are the applied strain components. Note that a factor of 2 has been included on the B_2 term, as tensorial strain components have been used in place of the engineering strain components commonly used in this expression (i.e., $e_{ij} = 2\varepsilon_{ij}$ for $i \neq j$).[54, 55] The tensorial strain components are now written in terms of the principal strains using a rank 2 tensor transformation

$$\varepsilon_{11} = \varepsilon_{avg} + \frac{1}{2}\varepsilon_b \cos(2\varphi_\varepsilon) \quad (3)$$

$$\varepsilon_{22} = \varepsilon_{avg} - \frac{1}{2}\varepsilon_b \cos(2\varphi_\varepsilon) \quad (4)$$

$$\varepsilon_{12} = \frac{1}{2}\varepsilon_b \sin(2\varphi_\varepsilon) \quad (5)$$

where φ_ε is the principal strain orientation shown on Figure 2b, $\varepsilon_{avg} = (\varepsilon_1 + \varepsilon_2)/2$ is the average strain, and $\varepsilon_b = \varepsilon_1 - \varepsilon_2$ is the biaxial strain .

Using equations 3 to 5 in equation 2 and converting to polar coordinates ($m_1 = \cos\theta$, and $m_2 = \sin\theta$), the energy expression becomes

$$U_{tot} = K_2 \cos(2\theta - \delta_s) + K_4 \cos(4\theta) \quad (6)$$

$$K_2 = \frac{1}{2}\varepsilon_b \sqrt{B_1^2 \cos^2(2\varphi_\varepsilon) + B_2^2 \sin^2(2\varphi_\varepsilon)} \quad (7)$$

$$K_4 = -\frac{1}{8}K_1^{MCA} \quad (8)$$

$$\tan(\delta_s) = \frac{B_2}{B_1} \tan(2\varphi_\varepsilon) \quad (9)$$

where K_2 and K_4 are the total second and fourth order anisotropy coefficients, and δ_s is the static rotation of the second order anisotropy with respect to the x-direction. Equation 6 is indicative of the fact that a conservative anisotropy energy can be expanded in a Fourier series ($U_{tot} = Re[\sum_n K_n e^{jn\theta}]$), and highlights the two and four fold rotational symmetry inherent to the cubic magnetoelastic and magnetocrystalline anisotropies, respectively. It should be noted that in these equations the second order anisotropy $K_2 \rightarrow K_2(t)$ is a time dependent function of the voltage induced biaxial strain ε_b , and independent of the average strain ε_{avg} . For an isotropic magnetoelastic material ($\lambda_{100} = \lambda_{111} \implies B_1 = B_2$) these expressions simplify to $K_2 = \varepsilon_b |B_1|/2$ and $\tan(\delta_s) = \tan(2\varphi_\varepsilon)$.

To locate the equilibrium configuration for an arbitrary input strain equation 6 is first converted

to a complex polynomial

$$U_{tot} = \text{Re} \left[K_2 e^{j(2\theta - \delta_s)} + K_4 e^{4j\theta} \right] \quad (10)$$

$$= \frac{1}{2} K_2 (pz^2 + \bar{p}\bar{z}^2) + \frac{1}{2} K_4 (z^4 + \bar{z}^4) \quad (11)$$

where $p = e^{-j\delta_s}$ and $z = e^{j\theta}$. The extrema of this expression are found using the Lagrange multiplier method to enforce the constraint that z has unit magnitude.

$$\mathcal{L}(z, \bar{z}, \lambda) = U_{tot}(z, \bar{z}) - \lambda(z\bar{z} - 1) \quad (12)$$

Combing the partial derivatives of equation 12 and making the substitution $R = K_2/K_4$, yields the 8th order complex polynomial

$$z^8 + \frac{1}{2} R p z^6 - \frac{1}{2} R \bar{p} \bar{z}^2 - 1 = 0 \quad (13)$$

which can be converted into a 4th order polynomial with the substitution $w = z^2$

$$w^4 + \frac{1}{2} R p w^3 - \frac{1}{2} R \bar{p} w - 1 = 0 \quad (14)$$

The roots of this equation provide the local extrema of the energy landscape.

Noting that R is the ratio of the second and fourth order anisotropies, it is easy to see when no strain is applied ($R = 0$) energy extrema are located at the 8th roots of unity ($w^4 = 1 \implies z^8 = 1 \implies \varphi = \pm n\pi/4$). Since the roots provide the location of both the maxima and minima of the fourth order cubic magnetocrystalline anisotropy, the solution for z has 8 angles per 2π radians when $R = 0$. The closed form solution for an arbitrary plane strain state is provided in the Supplementary Information.

B. Dynamic Analysis

This section analyzes the dynamics of the proposed motor using the Landau-Lifshitz-Gilbert (LLG) equation. The LLG equations is

$$\dot{\vec{m}} = -\gamma \vec{m} \times \vec{H}_{eff} - \alpha \vec{m} \times \dot{\vec{m}} \quad (15)$$

$$\vec{H}_{eff} = -\frac{1}{\mu_0 M_s} \frac{\partial U_{tot}}{\partial \vec{m}} \quad (16)$$

where the gyromagnetic ratio γ , Gilbert damping factor α , saturation magnetization M_s , and effective magnetic field \vec{H}_{eff} have been used. The effective field has one component for each of the energy expressions in Equation 1, with components

$$H_1 = -\frac{2}{\mu_0 M_s} [K_1^{mca} m_1 m_2^2 + B_1 m_1 \varepsilon_{11} + B_2 m_2 \varepsilon_{12}] \quad (17)$$

$$H_2 = -\frac{2}{\mu_0 M_s} [K_1^{mca} m_1^2 m_2 + B_1 m_2 \varepsilon_{22} + B_2 m_1 \varepsilon_{12}] \quad (18)$$

$$H_3 = -\frac{2}{\mu_0 M_s} \left[K_1^{mca} m_3 (m_1^2 + m_2^2) + K_2^{mca} m_1^2 m_2^2 m_3 + \frac{1}{2} \mu_0 M_s^2 m_3 \right] \quad (19)$$

where fields linear in m_3 have been retained, but all higher order contributions dropped.

The following analysis determines the strain amplitude and frequency required to cause rotational motion with constant angular velocity. It is assumed $m_1(t) = \cos \omega_0 t$, $m_2(t) = \sin \omega_0 t$, and that the biaxial strain follows a temporal dependence of $\varepsilon_b \propto \cos(\omega_\varepsilon t + \delta_d)$, where ω_ε is the mechanical driving frequency, and δ_d is dynamic phase difference between ε_b and m_i . It is also assumed that the mechanical strain is applied at twice the frequency of rotation $\omega_\varepsilon = 2\omega_0$, with one strain cycle causing a maximum of 180° rotation. This assumption will be justified after looking at the results of the quasi-static analysis.

Using the fact that the magnitude of the magnetic moment is conserved

$$\vec{m} \cdot \dot{\vec{m}} \approx m_1 \dot{m}_1 + m_2 \dot{m}_2 = 0 \quad (20)$$

where $\dot{\vec{m}}$ is calculated by inserting Equations 17 to 19 into Equation 15. This results in an expression of the form

$$A \sin(4\omega_\varepsilon t) + B \cos(4\omega_\varepsilon t) + C = 0 \quad (21)$$

where A, B, and C are functions of the material properties and operating conditions but independent of time. For the equality to hold for all time t, the coefficients A, B, and C must be identically zero, resulting in the operating conditions to achieve uniform rotation.

$$\omega_0 = \frac{\gamma K_1^{mca} B_1 B_2}{\alpha \mu_0 M_s (B_1^2 \cot(2\varphi_\varepsilon) + B_2^2 \tan(2\varphi_\varepsilon))} \quad (22)$$

$$\varepsilon_b = \pm \frac{K_1^{mca}}{B_1} \frac{\sec(2\varphi_\varepsilon)}{\sqrt{1 + B_2^2/B_1^2 \tan^2(2\varphi_\varepsilon)}} \quad (23)$$

$$\tan \delta_d = \frac{B_2}{B_1} \tan(2\varphi_\varepsilon) \quad (24)$$

From equations 22 and 23, it should be noted that the strain amplitude and frequency required for constant precession depend on both the material's anisotropy coefficients and orientation of the the principal strain. The dynamic phase difference between the strain and magnetic moment in equation 24 is equal to the static rotational offset of the magnetoelastic anisotropy provided in equation 9 (i.e. $\tan \delta_d = \tan \delta_s$). While equations 22 - 24 provide the conditions for constant angular velocity, applying a larger strain than ϵ_b will produce faster rotation, albeit with non-constant angular velocity. For isotropic magnetoelastic materials, these equations simplify to

$$\omega_0^{iso} = \frac{\gamma K_1^{mca}}{2\alpha\mu_0 M_s} \sin(4\varphi_\epsilon) \quad (25)$$

$$\epsilon_b^{iso} = \pm \frac{K_1^{mca}}{B_1} \quad (26)$$

$$\tan \delta_d^{iso} = \tan(2\varphi_\epsilon) \quad (27)$$

where the resulting frequency ω_0^{iso} increases with large crystalline anisotropies, and decreases with larger Gilbert damping and saturation magnetization. Additionally, the required strain amplitude ϵ_b^{iso} depends exclusively on the ratio of the crystalline and magnetoelastic anisotropy coefficients.

In addition to determining the constant precession conditions, the LLG equation was numerically simulated using Matlab, with a macrospin model based on the dynamic equations of motion. This was done to verify the calculations performed in this section, and to study the behavior of the motor at frequencies above and below ω_0 .

C. Motor Analysis

The analysis outlined in the preceding sections controls the rotational characteristics of the stator's magnetic moment. Assuming the uniformly magnetized rotor / stator can be treated as point dipoles, the stator's dipole field (due to magnetic moment $\vec{\mu}_1$) and force on the rotor (magnetic moment $\vec{\mu}_2$) due to the rotating moment of the stator is provided by

$$\vec{B}_1(\vec{\mu}_1, \vec{r}) = \frac{\mu_0}{4\pi r^3} (3(\vec{\mu}_1 \cdot \hat{r})\hat{r} - \vec{\mu}_1) \quad (28)$$

$$\vec{F}(\vec{\mu}_1, \vec{\mu}_2, \vec{r}) = \nabla \left(\vec{\mu}_2 \cdot \vec{B}_1(\vec{\mu}_1, \vec{r}) \right) \quad (29)$$

$$\begin{aligned} \therefore \vec{F}(\vec{\mu}_1, \vec{\mu}_2, \vec{r}) &= \frac{3\mu_0}{4\pi r^5} \left[(\vec{\mu}_1 \cdot \vec{r})\vec{\mu}_2 + (\vec{\mu}_2 \cdot \vec{r})\vec{\mu}_1 + \dots \right. \\ &\quad \left. (\vec{\mu}_1 \cdot \vec{\mu}_2)\vec{r} - \frac{5\vec{r}}{r^2} (\vec{\mu}_1 \cdot \vec{r})(\vec{\mu}_2 \cdot \vec{r}) \right] \quad (30) \end{aligned}$$

where $\vec{\mu}_\alpha = V_\alpha \vec{m}_\alpha M_s$ is the vector net magnetic moment of the rotor / stator, V_α is the volume, M_s the saturation magnetization, and \vec{m}_α is the direction cosine unit vector. Figure 2c shows the resulting force vectors at several locations around the stator. For a bead with magnetic moment of amplitude $|\vec{\mu}_2|$ located a distance r from the stator with moment amplitude $|\vec{\mu}_1|$, the maximum radial and tangential forces are given by Equations 31 and 32. The radial force is maximized when $\vec{r} \cdot \vec{\mu}_1 = 0$. The maximum tangential force occurs when the angle between the radius and $\vec{\mu}_1$ is $n\pi \pm \text{asin}(\sqrt{2})$.

$$|\vec{F}_r| = \frac{3\mu_0 |\vec{\mu}_1| |\vec{\mu}_2|}{2\pi r^4} \quad (31)$$

$$|\vec{F}_\phi| = |\vec{F}_r|/6 \quad (32)$$

For both of these equations it has been assumed that $\vec{\mu}_2 \parallel \vec{B}_1$.

III. RESULTS

This section presents the quasi-static energy equilibrium states, followed by results from the analytic and numerical treatment of the dynamic LLG response. Lastly, the relation between the dynamic response and overall motor power density will be discussed.

A. Quasi-Static Energy Analysis Results

Figure 3 shows the energy landscape for two different principal strain orientations (φ_ϵ). The x-axis represents the orientation of the in-plane magnetic moment θ , the y-axis shows the anisotropy ratio K_2/K_4 . Using Equations 7 and 8 positive K_2/K_4 values corresponds to tension and negative to compression. Surface color represents the energy for each given state calculated from Equation 6. The solid black lines trace the locations of energy minima, and dashed blue lines trace the locations of energy maxima. Both sets of lines correspond to the roots of the characteristic polynomial provided by Equation 14. Yellow stars indicate inflection points in the energy landscape which are locations where the system irreversibly flips from one energy minima to another.

For example, suppose the system in Figure 3a starts unstrained ($K_2/K_4 = 0$) at position 1, in the energy well at $\theta = 0$ radians. If tensile strain is applied (moving up the y-axis), then the system moves into a deeper energy well and doesn't rotate. If compressive strain is applied, the

system moves down the black line until $K_2/K_4 = -4$, at which point the magnetic moment non-deterministically flips to energy wells at $\theta = \pm\pi/2$ corresponding to positions 2a and 2b.

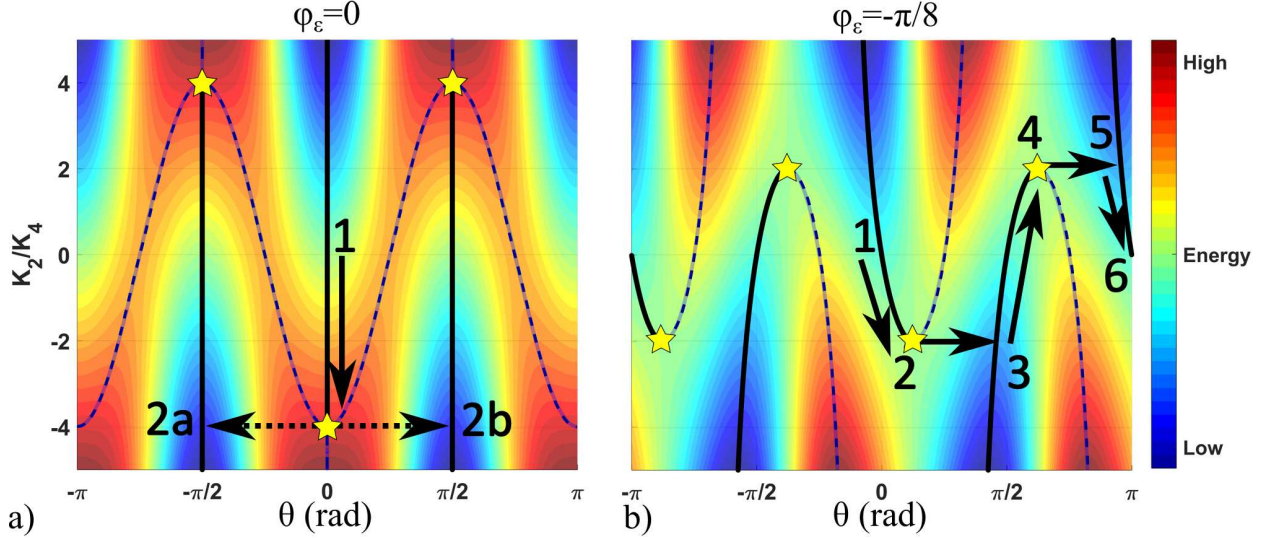


FIG. 3. Energy landscapes for two different principal strain orientations (φ_ε). Solid black lines track energy minima and dotted blue lines track energy maxima. Numbered black arrows correspond to loading pathways described in the text. a) Non-deterministic switching occurs when the $\varphi_\varepsilon = 0$. b) Deterministic switching occurs when $\varphi_\varepsilon = -\pi/8$

The case of deterministic switching is shown in Figure 3b, where $\varphi_\varepsilon = -\pi/8 = -22.5^\circ$. In this case starting unstrained in the energy well at position 1 ($\theta = 0$), compression again moves the system down the y-axis, but also slightly rotates it in the counter-clockwise direction until it reaches position 2. When $K_2/K_4 = -2$ an inflection point is encountered and the system deterministically flips to position 3, the energy well at $\theta \approx \pi/2$. Applying tension to the system until $K_2/K_4 = +2$ causes counter-clockwise rotation to the inflection point at position 4, and the system then jumps to position 5 ($\theta \approx \pi$), and removing the strain moves it to position 6. This example demonstrates how a single cycle of biaxial compression / tension causes the magnetic moment to deterministically rotate 180° . Therefore, two compression / tension cycles are needed to rotate a full 360° , and the system rotates at half the driving frequency (i.e., $\omega_\varepsilon = 2\omega_0$). This indicates that it is possible to deterministically rotate a magnetic moment using a magnetoelastic anisotropy with a fixed direction (i.e., allowing single electrode control).

Figure 4 shows the minimum anisotropy ratio required to rotate the magnetic moment. The upper solid blue line corresponds to the minimum ratio K_2/K_4 required to rotate, while the surface

color and insets indicate the direction of magnetic rotation. When $\varphi_\varepsilon = \pm n\pi/4$ the magnetic moment changes rotation directions. As $\varphi_\varepsilon = \pm n\pi/4$ corresponds the $\langle 100 \rangle$ and $\langle 110 \rangle$ family of directions, it becomes clear that non-deterministic rotation results when strain is applied along a crystallographic direction with large degree of symmetry. When $\varphi_\varepsilon = \pi/8 \pm n\pi/4$, the system is rotated with the minimum possible anisotropy ratio ($|K_2/K_4| = 2$). For isotropic magnetoelasticity, the minimum biaxial strain required to generate quasi-static rotation is

$$\min(|\varepsilon_b^{iso}|) = \begin{cases} \frac{K_1^{MCA}}{2B_1} & \text{for } \varphi_\varepsilon = \frac{\pi}{8} \pm \frac{n\pi}{4} \\ \frac{K_1^{MCA}}{B_1} & \text{for } \varphi_\varepsilon = \pm \frac{n\pi}{4} \end{cases} \quad (33)$$

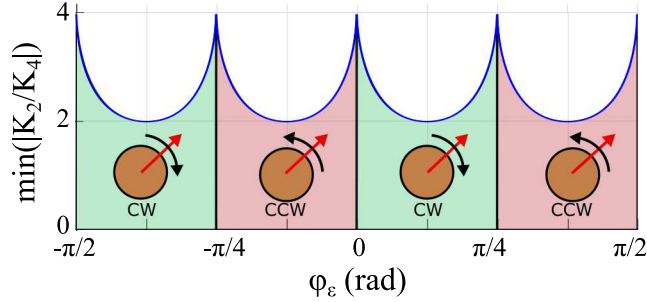


FIG. 4. Minimum anisotropy ratio required for rotation to occur. Deterministic rotation occurs as long as $\varphi_\varepsilon \neq n\pi/4$. The minimum flipping strain occurs when $\varphi_\varepsilon = \pi/8 \pm n\pi/4$

Applying strain at the appropriate angle reduces the flipping strain amplitude by a factor of 2, and therefore lowers the strain energy by a factor of 4 compared to the non-deterministic case. Based on Figure 4, a two input system generating principal strain states oriented at $\pm\pi/8$ will control bipolar operation. Lastly, while the fourfold anisotropy has been assumed to be crystalline in nature, shape anisotropy can also produce cubic anisotropies, as experimentally demonstrated by Lambson *et al.* [56].

B. Dynamic Results

Recall that the biaxial strain and frequency required to obtain constant precession were previously presented in Equations 22-24 for a general material, and Equations 25-27 for an isotropic material. For isotropic magnetoelasticity, the strain amplitude required for rotation at constant angular velocity matches the strain required for non-deterministic flipping to occur in the quasi-static analysis ($\varepsilon_b^{iso} = \pm \frac{K_1}{B_1}$). Furthermore, the rotational frequency depends on the orientation of

the applied strain ($\omega_0^{iso} \propto \sin(4\varphi_\varepsilon)$). When the strain is applied at an angle $\varphi_\varepsilon = \pm n\pi/4$, the angular velocity $\omega_0 = 0$. Therefore, when $\varphi_\varepsilon = \pm n\pi/4$, both the quasi-static and dynamic analyses converge to predicting $\varepsilon_b^{iso} = \pm \frac{K_1}{B_1}$, with zero angular frequency (i.e., random non-deterministic rotations). This demonstrates consistency between the static and dynamic solutions. Consistency was further checked by numerically simulating the motor stator element operating at several strain amplitudes and frequencies.

Figure 5 shows the frequency response of this motor stator for quasi static and dynamic operation at 7 different frequencies for two full cycles of tension / compression. Parts a)-c) show the impact of using three different biaxial strain amplitudes. At quasi-static rates (i.e., calculated tracking energy equilibrium orientations), the magnetic moment exhibits ratchet-like behavior, with abrupt switches every time the minimum switching strain is reached ($\varepsilon_b = \pm \frac{K_1^{MCA}}{2B_1}$). If a larger strain is applied (shown in part b and c) the magnet undergoes a small period of clockwise motion (i.e., temporarily changes direction), as would be expected from Figure 3.

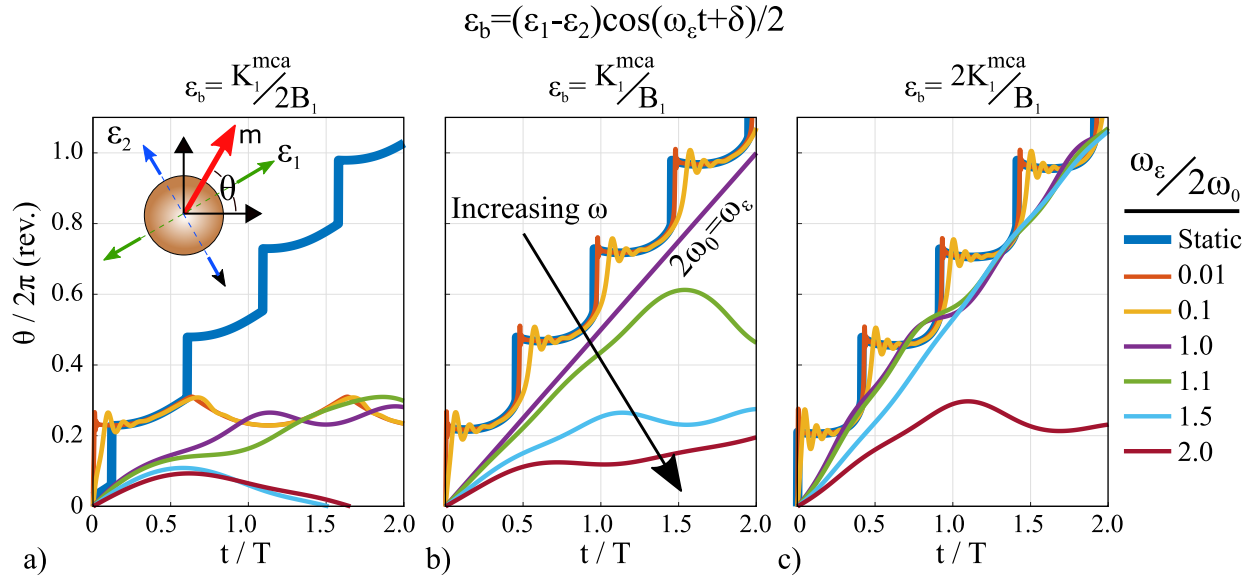


FIG. 5. Magnetic revolutions vs time for a motor with isotropic magnetoelasticity and $\varphi_\varepsilon = -\pi/8$ at several driving frequencies. Results are shown temporally normalized with respect to the period of the strain signal ($T = 2\pi/\omega_\varepsilon$). Simulations are shown for Gilbert damping $\alpha = 0.01$. Specific material properties and relevant model terms are presented in Table I.

Figure 5a indicates that the minimum predicted strain generates continuous rotation only for quasi-static behavior. Operating at $\omega_\varepsilon/2\omega_0 \geq 0.01$ when $\varepsilon_b = \pm \frac{K_1^{MCA}}{2B_1}$ results in minor fluctuations about a fixed orientation. While not depicted in Figure 5a, it was observed that increasing the

strain to $\epsilon_b = 1.01 \cdot \frac{K_1^{MCA}}{2B_1}$ generated successful rotation for $\omega_\epsilon/2\omega_0 \leq 0.01$, indicating the minimum flipping strain is valid at frequencies that are small compared to ω_0 . The under damped yellow line in Figure 5b indicates that if $\epsilon_b = \pm \frac{K_1^{MCA}}{B_1}$, quasi-static performance is maintained up to $\omega_\epsilon/2\omega_0 \leq 0.1$. Furthermore, the case where $\epsilon_b = \pm \frac{K_1^{MCA}}{B_1}$ and $\omega_\epsilon = 2\omega_0$ resulted in constant angular velocity as analytically predicted by Equation 25 (shown with the straight purple line). If the frequency ω_ϵ is further increased by 10%, the motor fails to deterministically rotate.

Figure 5c shows that when larger strains are applied, larger operational frequencies can be attained. Doubling the strain from part b results in constant precession with a 50% increase in rotational frequency. It should be noted that this increase is not directly proportional, as operating with double the strain amplitude did not enable operation at twice the frequency. The data in Figure 5 was reproduced for a variety of Gilbert damping coefficients from 0.01 to 0.1, with Figure 5 showing results for $\alpha = 0.01$. They were found to provide qualitatively similar results, albeit with the highest damping leading to smaller overshoot and smoother overall behavior.

Table I provides a list of magnetic materials along with their relevant properties, predicted minimum strain for quasi-static operation, and operational frequency for constant precession. This table makes it abundantly clear that the ratio K_1^{mca}/B_1 is the key metric to reduce the applied strain amplitude. Moderately magnetoelastic materials like Ni and Ni₅₅Fe₄₅ require the smallest strains ($90 \leq \epsilon_b \leq 360$ ppm) due to their low crystalline anisotropies. On the other hand, an epitaxially grown thin film of Terfenol-D (Tb_{0.3}Dy_{0.7}Fe₂) has the largest magnetoelastic anisotropy coefficient B_1 , but due to a large crystalline anisotropy K_1 would require $\epsilon_b \approx 3,300$ ppm to rotate, which would be challenging for most ferroelectric materials even at quasi-static frequencies.

The frequencies listed in Table I range from 1 GHz to 1 THz, and indicate the magnetic dynamics of these motors will have minimal effect once mechanical losses are accounted for. Also recall that quasi-static behavior was seen to persist up to 1% of ω_0 in Figure 5b. That means these motors are magnetically quasi-static at frequencies up to 10s of MHz (i.e., in energy equilibrium), providing broadband operation. It should be noted that the Gilbert damping parameter was assumed to be $\alpha = 0.01$ for all the listed materials, while larger values may be encountered. At the frequencies predicted in this paper, the coupled mechanical behavior of the motor will be important, and needs to be incorporated for more thorough and accurate predictions (i.e., using a fully coupled modeling approach), however that is consider outside the scope of the present article.

TABLE I. Comparison of the minimum strain required for deterministic control of a variety of magnetoelectric materials.

Material	$\mu_0 M_s$ (T)	K_1 (kJ/m ³)	B_1 ^{a b} (MJ/m ³)	$\epsilon_b^{\min} = \frac{K_1}{2B_1}$ (ppm)	$\omega_0/2\pi = \frac{\gamma K_1^{\text{mca}}}{4\pi\alpha\mu_0 M_s}$ ^c (GHz)	Source
Ni-FCC	0.6	-4.5	6.2	363	13	[55]
Co-FCC	1.8	-120	-16	3,750	117	[55]
Co-HCP	1.8	350	6	29,167	342	[55]
Fe-BCC	2.1	48	-2.9	8,276	40	[55]
Fe ₈₁ Ga ₁₉ ^d	1.4	17.5	22.4	391	22	[57]
Tb _{0.3} Dy _{0.7} Fe ₂ ^e	0.9	-525	-80	3,280	1,027	[58]
Ni ₅₅ Fe ₄₅	1.6	1	5.5	90	1.1	[55]

^a $B_1 = -\frac{3}{2}\lambda_{100}(C_{11} - C_{12})$

^b For isotropic materials $(C_{11} - C_{12}) = E/(1 + 2\nu)$

^c Assumed $\alpha = 0.01$ for all materials

^d Assuming $E=75$ GPa, $\nu = 0.3$

^e Epitaxial thin film

C. Multiferroic Motor Power Density

The last focus of this paper is to determine approximate performance bounds of a mechanically lossless bead-on-on-a-disk motor using the developed control scheme. The material from Table I requiring the smallest strain is Ni₅₅Fe₄₅, which is the focus of this section. A motor with stator radius $r_1 = 100$ nm, thickness $t = 10$ nm and rotor (bead) radius of $r_2 = 10$ nm was simulated, with dimensions chosen to keep the stator a single domain.

In the absence of mechanical losses, the upper bound for the rotary motor's frequency is dictated by inertial forces. In other words, if the rotary motor is operated at too large a frequency, the bead will be flung away from the stator due to its own momentum. While this may be useful in some circumstances, it does limit the maximum frequency to

$$|\vec{F}_r| = m\omega^2 r \quad (34)$$

$$\therefore f_{\max} = \frac{1}{2\pi} \sqrt{\frac{3\mu_0 |\vec{\mu}_1| |\vec{\mu}_2|}{2\pi m r^5}} \quad (35)$$

where Equation 31 has been used. For the specified motor, $f_{\max} \approx 9.7$ MHz, which corresponds to

a linear velocity $v \approx 6.1 \text{ m s}^{-1}$. Based on the results from Table I, this is roughly 100 times slower than $\omega_0^{iso}/2\pi$. However, this low frequency / velocity is a limit of this specific rotary motor design, and not an intrinsic limit for multiferroic motors. For instance, a linear motor can be made that overcomes these inertial limitations.

The linear motor shown in Figure 6a overcomes the frequency limitations of the rotary motor by not forcing the bead to change directions (i.e., it works with the bead's inertia). This motor can be fabricated by patterning rotary motors adjacent to each other, and optionally etching a trough, or depositing a wall / barrier on top of them to physically guide the bead. As inertial effects are now advantageous, and help pass the bead from one disc to the next, in the limit of zero fluidic drag the bead can be propelled as fast as the stator's magnetic moment can rotate. For a $\text{Ni}_{55}\text{Fe}_{45}$

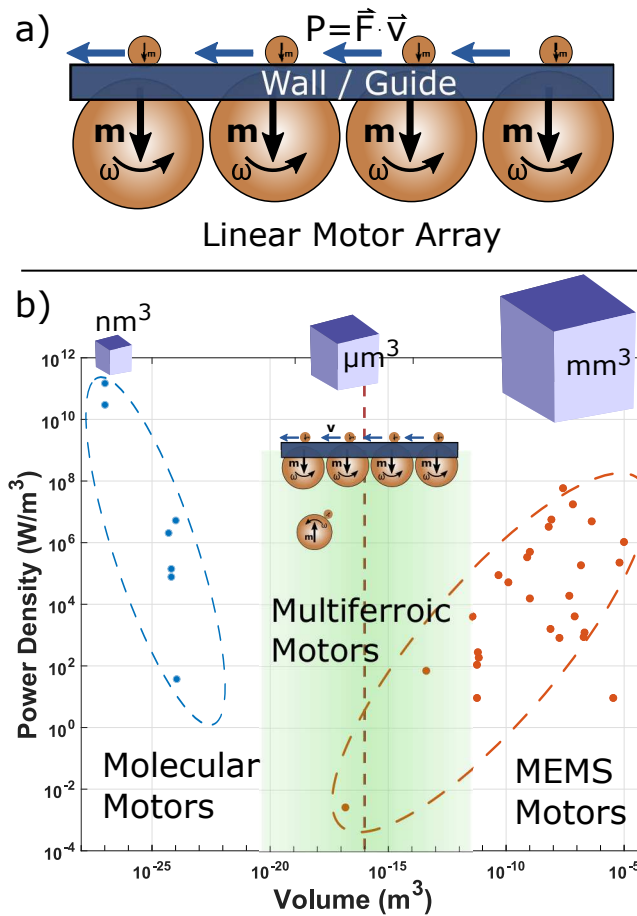


FIG. 6. Updated power density chart now showing approximate upper bounds for both rotary and linear multiferroic bead-on-a-disk motors.[2–36]

motor with the dimensions listed above, the magnetic moment is able to precess at a frequency of $f \approx 1.1 \text{ GHz}$, which corresponds to a linear velocity of $v \approx 700 \text{ m s}^{-1}$.

Based on the attainable speed, and dipole forces driving the motion, approximate bounds on the maximum power density of the rotary and linear motors can be calculated. Assuming the vibrating piezoelectric substrate is $100\ \mu\text{m}$ thick, the rotary motor volume is on the order of 10^{-18}m^3 . The maximum rotary power density is predicted to be $4.4\ \text{MW}/\text{m}^3$, and the maximum linear power density is predicted to be over two orders of magnitude higher at $470\ \text{MW}/\text{m}^3$. The increase in power density is due entirely to the higher operational frequency of the linear motor. These predictions provide approximate upper bounds for multiferroic bead-on-a-disc motors with negligible mechanical losses.

Figure 6 shows the power density chart now updated with predictions for the rotary and linear multiferroic motors. The multiferroic motor concept fills the void left by previous technologies, providing a power dense motor with μm^3 dimensions. The upper limit to this boundary corresponds to motors operating at GHz frequencies, with lower power densities achieved by decreasing the operational frequency. Furthermore, the linear motor is able to scale up in size while still maintaining the same power density. This is accomplished in practice by creating particle conveyor belts with the linear motor that have relatively large lengths.

To close, we comment on a key simplifying assumption used in this analysis, namely the absence of mechanical losses including friction, stiction, and fluidic drag. Operation anywhere close to these large frequencies will involve mechanical losses, which need to be a key focus of future studies. This analysis highlights the key fact that the intrinsic magnetic dynamics are sufficiently fast that the stator element is likely to always be in a state of energy equilibrium during actual use. This suggests two very important motor characteristics. One, since stator speed is not a fundamental limit of these devices, future researchers would be prudent to focus on designs moving magnetic structures like domain walls and onion states with large magnetic gradients that amplify dipolar forces. Such a structure has been analyzed by Sohn *et al.* [38], who dragged a $1\ \mu\text{m}$ diameter magnetic bead at speeds near $1\ \text{mm s}^{-1}$. That motion likely achieved a power density on the order of $10\ \text{kW}/\text{m}^3$, a point right in the middle of the power densities predicted in Figure 6. Second, the expected quasi-static behavior of the stator also implies its rotational behavior will be similar to a stepper motor, with abrupt transitions. This characteristic would complicate the use of a rotary motor design, with rapid changes shaking the beads loose. However a linear motor should still work even with abrupt transitions, as the bead's own momentum becomes an aid to continued motion.

IV. CONCLUSION

This work has demonstrated how controlling the relative orientation of a two-fold anisotropy (magnetoelasticity) with a four-fold anisotropy (e.g., cubic MCA) can achieve single electrode control of deterministic 360 degree magnetic rotations. Bounds were determined for the strain required to generate continuous rotation for quasi-static and dynamic operation, and the conditions for achieving constant angular precession were determined. For currently available materials, strains as low as 90 ppm are predicted to enable the operation of these motors, and large frequencies are attainable in the absence of fluidic damping. A novel linear motor was also proposed, that avoids some limitations of the rotary bead-on-a-disk motor. The proposed motors are predicted to have large power densities at a size scale where no power dense alternative technologies currently exist, and offer a promising new technology for further exploration.

ACKNOWLEDGMENTS

This research was supported by the NSF Nanosystems Engineering Research Center for Translational Applications of Nanoscale Multiferroic Systems (TANMS) Cooperative Agreement Award (No. EEC-1160504).

-
- [1] J. P. Joule, "On a new class of magnetic forces," **8**, 219–224 (); James Prescott Joule, *The Scientific Papers of James Prescott Joule*, Vol. 1 (Cambridge University Press).
 - [2] Y. C. Tai, L. S. Fan, and R. S. Muller, "IC-processed micro-motors: design, technology, and testing," in *IEEE Micro Electro Mechanical Systems, 1989, Proceedings, An Investigation of Micro Structures, Sensors, Actuators*, pp. 1–6.
 - [3] U. Wallrabe, P. Bley, B. Krevet, W. Menz, and J. Mohr, "Theoretical and experimental results of an electrostatic micro motor with large gear ratio fabricated by the LIGA process," in *[1992] Proceedings IEEE Micro Electro Mechanical Systems*, pp. 139–140.
 - [4] Yu-Chong Tai and Richard S. Muller, "IC-processed electrostatic synchronous micromotors," *A Special Issue Devoted to Micromechanics*, **20**, 49–55.
 - [5] Daniel Kuang-Chen Liu, James Friend, and Leslie Yeo, "A brief review of actuation at the micro-scale using electrostatics, electromagnetics and piezoelectric ultrasonics," **31**, 115–123 ().

- [6] S. C. Jacobsen, R. H. Price, J. E. Wood, T. H. Rytting, and M. Rafaelof, "The wobble motor: design, fabrication and testing of an eccentric-motion electrostatic microactuator," in *1989 International Conference on Robotics and Automation Proceedings*, pp. 1536–1546 vol.3.
- [7] N. Ghalichechian, A. Modafe, M. I. Beyaz, and R. Ghodssi, "Design, fabrication, and characterization of a rotary micromotor supported on microball bearings," **17**, 632–642.
- [8] C. Livermore, A. R. Forte, T. Lyszczarz, S. D. Umans, A. A. Ayon, and J. H. Lang, "A high-power MEMS electric induction motor," **13**, 465–471.
- [9] M. Glickman, P. Tseng, J. Harrison, T. Niblock, I. B. Goldberg, and J. W. Judy, "High-performance lateral-actuating magnetic MEMS switch," **20**, 842–851.
- [10] Pauline J. Chang, Frank W. Chang, Michelle C. Yuen, Robert Otilar, and David A. Horsley, "Force measurements of a magnetic micro actuator proposed for a microvalve array," **24**, 034005.
- [11] N. Achotte, P. A. Gilles, O. Cugat, J. Delamare, P. Gaud, and C. Dieppedale, "Planar brushless magnetic micromotors," **15**, 1001–1014.
- [12] Kenjiro Takemura, Hiroto Kozuki, Kazuya Edamura, and Shinichi Yokota, "A micromotor using electro-conjugate fluidimprovement of motor performance by using saw-toothed electrode series," **140**, 131–137.
- [13] Takefumi Kanda, Akira Makino, Tomohisa Ono, Koichi Suzumori, Takeshi Morita, and Minoru Kuribayashi Kurosawa, "A micro ultrasonic motor using a micro-machined cylindrical bulk PZT transducer," **127**, 131–138.
- [14] B. Watson, J. Friend, and L. Yeo, "Micromotor of less than 1 mm³ volume for in vivo medical procedures," in *2009 Third International Conference on Quantum, Nano and Micro Technologies*, pp. 81–85.
- [15] T. Mashimo, "Performance evaluation of a micro ultrasonic motor using a one-cubic-millimeter stator," **62**, 1819–1826.
- [16] Anita M. Flynn, "Performance of ultrasonic mini-motors using design of experiments," **7**, 286.
- [17] Toshiiku Sashida and Takashi Kenj, *An introduction to ultrasonic motors* (Oxford : Clarendon Press ; New York : Oxford University Press).
- [18] Takeshi Morita, Minoru K. Kurosawa, and Toshiro Higuchi, "A cylindrical micro-ultrasonic motor (stator transducer size: 1.4 mm in diameter and 5.0 mm long)," **38**, 33–36.
- [19] Serra Cagatay, Burhanettin Koc, Paul Moses, and Kenji Uchino, "A piezoelectric micromotor with a stator of 1.6 mm and L=4 mm using bulk PZT," **43**, 1429.

- [20] J. Satonobu, D. Lee, K. Nakamura, and S. Ueha, "Improvement of the longitudinal vibration system for the hybrid transducer ultrasonic motor," **47**, 216–221.
- [21] Atsuyuki Suzuki and Jiromaru Tsujino, "Load characteristics of ultrasonic motors with a longitudinal-torsional converter and various nonlinear springs for inducing static pressure," **41**, 3267.
- [22] B. Watson, J. Friend, and L. Yeo, "Piezoelectric ultrasonic resonant motor with stator diameter less than 250 μm : the proteus motor," **19**, 022001 ().
- [23] M. De Volder, A. J. M. Moers, and D. Reynaerts, "Fabrication and control of miniature McKibben actuators," **166**, 111–116 ().
- [24] Sebastian Btefishch, Volker Seidemann, and Stephanus Bttgenbach, "Novel micro-pneumatic actuator for MEMS," Selected papers from Eurosenors XV, **9798**, 638–645.
- [25] Satoshi Konishi, Fumie Kawai, and Pierre Cusin, "Thin flexible end-effector using pneumatic balloon actuator," Special Issue: Micromechanics Section of Sensors and Actuators, based on contributions revised from the T
- [26] M. De Volder, J. Coosemans, R. Puers, and D. Reynaerts, "Characterization and control of a pneumatic microactuator with an integrated inductive position sensor," **141**, 192–200 ().
- [27] U. Gebhard, H. Hein, E. Just, and P. Ruther, "Combination of a fluidic micro-oscillator and micro-actuator in LIGA-technique for medical application," in *1997 International Conference on Solid State Sensors and Actuators, 1997. TRANSDUCERS '97 Chicago*, Vol. 2, pp. 761–764 vol.2.
- [28] Ming Liu, Thomas Zentgraf, Yongmin Liu, Guy Bartal, and Xiang Zhang, "A nano-scale light-driven plasmonic motor," in *Conference on Lasers and Electro-Optics 2010 (2010)*, paper QPDA11 (Optical Society of America) p. QPDA11.
- [29] Kwanoh Kim, Xiaobin Xu, Jianhe Guo, and D. L. Fan, "Ultrahigh-speed rotating nanoelectromechanical system devices assembled from nanoscale building blocks," **5**, 3632.
- [30] Vincenzo Balzani, Miguel Clemente-Len, Alberto Credi, Beln Ferrer, Margherita Venturi, Amar H. Flood, and J. Fraser Stoddart, "Autonomous artificial nanomotor powered by sunlight," **103**, 1178–1183.
- [31] Perrine Lussis, Tiziana Svaldo-Lanero, Andrea Bertocco, Charles-Andr Fustin, David A. Leigh, and Anne-Sophie Duwez, "A single synthetic small molecule that generates force against a load," **6**, 553–557.
- [32] B. C. Regan, S. Aloni, K. Jensen, R. O. Ritchie, and A. Zettl, "Nanocrystal-powered nanomotor," **5**, 1730–1733.

- [33] Huaizhi Kang, Haipeng Liu, Joseph A. Phillips, Zehui Cao, Youngmi Kim, Yan Chen, Zunyi Yang, Jianwei Li, and Weihong Tan, “Single-DNA molecule nanomotor regulated by photons,” **9**, 2690–2696.
- [34] Derek N. Fuller, Dorian M. Raymer, Vishal I. Kottadiel, Venigalla B. Rao, and Douglas E. Smith, “Single phage t4 DNA packaging motors exhibit large force generation, high velocity, and dynamic variability,” **104**, 16868–16873.
- [35] Wolfgang Junge, Hendrik Sielaff, and Siegfried Engelbrecht, “Torque generation and elastic power transmission in the rotary FOF1-ATPase,” **459**, 364–370.
- [36] Oliver Pnke, Dmitry A. Cherepanov, Karin Gumbiowski, Siegfried Engelbrecht, and Wolfgang Junge, “Viscoelastic dynamics of actin filaments coupled to rotary f-ATPase: Angular torque profile of the enzyme,” **81**, 1220–1233.
- [37] Coleman Murray, Edward Pao, Peter Tseng, Shayan Aftab, Rajan Kulkarni, Matthew Rettig, and Dino Di Carlo, “Quantitative magnetic separation of particles and cells using gradient magnetic ratcheting,” **12**, 1891–1899.
- [38] Hyunmin Sohn, Mark E. Nowakowski, Cheng yen Liang, Joshua L. Hockel, Kyle Wetzlar, Scott Keller, Brenda M. McLellan, Matthew A. Marcus, Andrew Doran, Anthony Young, Mathias Klaui, Gregory P. Carman, Jeffrey Bokor, and Robert N. Candler, “Electrically driven magnetic domain wall rotation in multiferroic heterostructures to manipulate suspended on-chip magnetic particles,” **9**, 4814–4826.
- [39] Noel DSouza, Mohammad Salehi Fashami, Supriyo Bandyopadhyay, and Jayasimha Atulasimha, “Experimental clocking of nanomagnets with strain for ultralow power boolean logic,” **16**, 1069–1075.
- [40] N. D’Souza, J. Atulasimha, and S. Bandyopadhyay, “Energy-efficient bennett clocking scheme for four-state multiferroic logic,” **11**, 418–425.
- [41] D. Labanowski, A. Jung, and S. Salahuddin, “Effect of magnetoelastic film thickness on power absorption in acoustically driven ferromagnetic resonance,” *Applied Physics Letters* **111**, 102904 (2017), <http://dx.doi.org/10.1063/1.4994933>.
- [42] C Chen, A Barra, A Mal, G Carman, and A Sepulveda, “Voltage induced mechanical/spin wave propagation over long distances,” *Applied Physics Letters* **110**, 072401 (2017).
- [43] Tao Wu, Alexandre Bur, Joshua L Hockel, Kin Wong, Tien-Kan Chung, and Gregory P Carman, “Electrical and mechanical manipulation of ferromagnetic properties in polycrystalline nickel thin

- film,” **2**, 6000104–6000104.
- [44] J. L. Hockel, *Deterministic Magnetization Control by Magnetoelastic Anisotropy and its Dependence on Geometry and Scale*, Ph.D. thesis (2013).
- [45] Jizhai Cui, Joshua L. Hockel, Paul K. Nordeen, David M. Pisani, Cheng yen Liang, Gregory P. Carman, and Christopher S. Lynch, “A method to control magnetism in individual strain-mediated magnetoelectric islands,” **103**, 232905 ().
- [46] Jizhai Cui, Cheng-Yen Liang, Elizabeth A. Paisley, Abdon Sepulveda, Jon F. Ihlefeld, Gregory P. Carman, and Christopher S. Lynch, “Generation of localized strain in a thin film piezoelectric to control individual magnetoelectric heterostructures,” **107**, 092903 ().
- [47] Cheng-Yen Liang, Scott M Keller, Abdon E Sepulveda, Alexandre Bur, Wei-Yang Sun, Kyle Wetzlar, and Gregory P Carman, “Modeling of magnetoelastic nanostructures with a fully coupled mechanical-micromagnetic model,” *Nanotechnology* **25**, 435701 (2014).
- [48] Cheng-Yen Liang, Abdon E. Sepulveda, Daniel Hoff, Scott M. Keller, and Gregory P. Carman, “Strain-mediated deterministic control of 360 degree domain wall motion in magnetoelastic nanorings,” **118**, 174101.
- [49] Hyunmin Sohn, Cheng yen Liang, Mark E. Nowakowski, Yongha Hwang, Seungoh Han, Jeffrey Bokor, Gregory P. Carman, and Robert N. Candler, “Deterministic multi-step rotation of magnetic single-domain state in nickel nanodisks using multiferroic magnetoelastic coupling,” *Journal of Magnetism and Magnetic Materials* **439**, 196 – 202 (2017).
- [50] Qianchang Wang, Xu Li, Cheng Yen Liang, Anthony Barra, John P Domann, Chris Lynch, Abdon E. Sepulveda, and Greg Carman, “Strain-mediated 180 degree switching in CoFeB and terfenol-d nanodots with perpendicular magnetic anisotropy,” **110**, 102903 (2017).
- [51] J. J. Wang, J. M. Hu, J. Ma, J. X. Zhang, L. Q. Chen, and C. W. Nan, “Full 180 magnetization reversal with electric fields,” **4**, 7507.
- [52] Ren-Ci Peng, J. J. Wang, Jia-Mian Hu, Long-Qing Chen, and Ce-Wen Nan, “Electric-field-driven magnetization reversal in square-shaped nanomagnet-based multiferroic heterostructure,” **106**, 142901.
- [53] Jizhai Cui, Scott M. Keller, Cheng-Yen Liang, Gregory P. Carman, and Christopher S. Lynch, “Nanoscale magnetic ratchets based on shape anisotropy,” **28** (), 10.1088/1361-6528/aa56d4.
- [54] Soshin Chikazumi, *Physics of Ferromagnetism 2e*, 94 (Oxford University Press, 2009).
- [55] Robert C OHandley, *Modern magnetic materials: principles and applications*, Vol. 1 (Wiley).

- [56] Brian Lambson, Zheng Gu, Morgan Monroe, Scott Dhuey, Andreas Scholl, and Jeffrey Bokor, “Concave nanomagnets: Investigation of anisotropy properties and applications to nanomagnetic logic,” *Applied Physics A: Materials Science and Processing* **111**, 413–421 (2013).
- [57] Jayasimha Atulasimha and Alison B Flatau, “A review of magnetostrictive iron-gallium alloys,” *Smart Materials and Structures* **20**, 043001 (2011).
- [58] C de la Fuente, J I Arnaudas, L Benito, M Ciria, A del Moral, C Dufour, and K Dumesnil, “Magneto-crystalline anisotropy in a (110) (tb 0.27 dy 0.73)fe 2 thin-film,” *Journal of Physics: Condensed Matter* **16**, 2959 (2004).

V. SUPPLEMENTARY INFORMATION

A. Proof Ellipsoidal Magnets Can Not Enable 360° Deterministic Single Input Control

Several previous modeling and experimental studies have focused on controlling magnetic structures with elliptical shapes. However, the use of ellipsoidal structures alone can not result in deterministic 360° rotations if the principal strain axis is stationary (i.e., for single input control). While it should be clear from physical arguments that combining magnetoelasticity and a uniaxial shape anisotropy (i.e., using an ellipse) is limited to $\leq 90^\circ$ rotations, we provide the following proof for completeness.

Assuming without loss of generality that the ellipse has a long axis in the y-direction, and that the magnetization is constrained to lie in the xy plane, the demagnetization energy is

$$U_{demag} = K_u \cos(2\theta) \quad (36)$$

where $K_u = -(N_y - N_x)/2$ is the uniaxial demagnetization energy coefficient which depends on the x and y values of the demagnetization tensor N_x and N_y . Combining this energy with the arguments that lead to Equation 6, magnetoelastic rotations in an elliptical shape are governed by the total energy expression.

$$U_{tot} = K_u \cos(2\theta) + \frac{1}{2}\epsilon_b B_1 \cos(2\varphi_\epsilon) \cos(2\theta) + \frac{1}{2}\epsilon_b B_2 \sin(2\varphi_\epsilon) \sin(2\theta) \quad (37)$$

with φ_ϵ still the principal strain orientation.

Equation 37 is simply the addition of sin and cos terms of the same frequency. Of course, $A \cos(n\theta) + B \sin(n\theta) = C \cos(n\theta - \delta)$, where $C = \text{sgn}(A) \sqrt{A^2 + B^2}$, and $\delta = \tan(B/A)$. Therefore

the energy can be written as a single uniaxial anisotropy

$$U_{tot} = K_{tot} \cos(2\theta - \delta) \quad (38)$$

$$K_{tot} = \text{sgn} \left(\frac{1}{2} \varepsilon_b B_1 \cos(2\varphi_\varepsilon) + K_u \right) \dots$$

$$\sqrt{\left(\frac{1}{2} \varepsilon_b B_1 \cos(2\varphi_\varepsilon) + K_u \right)^2 + \left(\frac{1}{2} \varepsilon_b B_2 \sin(2\varphi_\varepsilon) \right)^2} \quad (39)$$

$$\tan(\delta) = \frac{\varepsilon_b B_2 \sin(2\varphi_\varepsilon)/2}{K_u + \varepsilon_b B_1 \cos(2\varphi_\varepsilon)/2} \quad (40)$$

This energy has local extrema when $\theta = \pm n\pi/4 + \delta/2$, which is controlled by δ , while the sign of K_{tot} determines whether the locations is a maxima or minima. The equation for $\tan(\delta)$ can be simplified to

$$\tan(\delta) = \frac{B_2 \sin(2\varphi_\varepsilon)}{2K_u/\varepsilon_b + B_1 \cos(2\varphi_\varepsilon)} \quad (41)$$

In this equation, the only dynamic variable is the biaxial strain ε_b . Examining $\tan(\delta)$ as ε_b approaches several limiting values reveals

$$\lim_{\varepsilon_b \rightarrow 0} (\tan(\delta)) = 0 \quad (42)$$

$$\lim_{\varepsilon_b \rightarrow \pm\infty} (\tan(\delta)) = \frac{B_2}{B_1} \tan(2\varphi_\varepsilon) \quad (43)$$

The changes in the total anisotropy orientation are constrained to $0 \leq |\tan(\delta)| \leq |B_2/B_1 \tan(2\varphi_\varepsilon)|$, with the sign controlled by the material properties and orientation of the principal strains. While the total anisotropy has the same orientation for large $\pm\varepsilon_b$, the sign of K_{tot} will change. In one case δ specifies an energy minimum, while in the other δ specifies an energy maximum, with minimum rotated 90° . Therefore, a maximum repeatable rotation of 90° can be achieved by combining an elliptical element with a magnetoelastic anisotropy where the principal strain orientation is constant.

B. Static Energy Analysis: Complex Roots

The roots of equation 14 were determined using Mathematica, and are provided with the closed form expression:

$$w_i(s_1, s_2, s_3) = -\frac{A}{4} + s_1 \frac{1}{2} \sqrt{\frac{A^2}{4} + d} + \dots$$

$$s_2 \frac{1}{2} \left[\frac{A^2}{2} + \left(\frac{2}{3c} \right)^{1/3} a - \left(\frac{c}{18} \right)^{1/3} + s_3 \frac{A^3 + 8B}{4\sqrt{\frac{A^2}{4} + d}} \right] \quad (44)$$

$$A = \frac{Rp}{2} \quad (45)$$

$$B = -\frac{R\bar{p}}{2} \quad (46)$$

$$a = 4 + AB \quad (47)$$

$$b = A^2 - B^2 \quad (48)$$

$$c = -9b + \sqrt{12a^3 + 81b^2} \quad (49)$$

$$d = \left(\frac{1}{36c} \right)^{1/3} (-23^{1/3}a + (2c^2)^{1/3}) \quad (50)$$

where the s_i represent sign changes from one root to the next. The roots are provided by

$$w_1 = w_i(-1, -1, +1) \quad (51)$$

$$w_2 = w_i(-1, +1, +1) \quad (52)$$

$$w_3 = w_i(+1, -1, -1) \quad (53)$$

$$w_4 = w_i(+1, +1, -1) \quad (54)$$

$$z_i = \pm \sqrt{w_i} \quad (55)$$